Deep-underground dark matter search with a COSINUS detector prototype

G. Angloher,[1] M. R. Bharadwaj,[1,*] I. Dafinei,[2,3] N. Di Marco,[2,4] L. Einfalt,[5,6,†] F. Ferroni,[2,3] S. Fichtinger,[5] A. Filipponi,[4,7] T. Frank,[1] M. Friedl,[5] A. Fuss,[5,6] Z. Ge,[8] M. Heikinheimo,[9] M. N. Hughes,[1] K. Huitu,[9] M. Kellermann,[1,‡] R. Maji,[5,6] M. Mancuso,[1] L. Pagnanini,[2,4] F. Petricca,[1] S. Pirro,[4] F. Pröbst,[1] G. Profeta,[4,7] A. Puiu,[2,4] F. Reindl,[5,6] K. Schäffner,[1] J. Schieck,[5,6] D. Schmiedmayer,[5,6] C. Schwertner,[5,6] K. Shera,[1] M. Stahlberg,[1] A. Stendahl,[9] M. Stukel,[2,4] C. Tresca,[4,10] F. Wagner,[5] S. Yue,[8] V. Zema,[1] and Y. Zhu[8]

(COSINUS Collaboration)

[1]*Max-Planck-Institut für Physik, 85748 Garching, Germany*
[2]*Gran Sasso Science Institute, 67100 L'Aquila, Italy*
[3]*INFN—Sezione di Roma, 00185 Roma, Italy*
[4]*INFN—Laboratori Nazionali del Gran Sasso, 67010 Assergi, Italy*
[5]*Institut für Hochenergiephysik der Österreichischen Akademie der Wissenschaften, 1050 Wien, Austria*
[6]*Atominstitut, Technische Universität Wien, 1020 Wien, Austria*
[7]*Dipartimento di Scienze Fisiche e Chimiche, Università degli Studi dell'Aquila, 67100 L'Aquila, Italy*
[8]*SICCAS - Shanghai Institute of Ceramics, 201899 Shanghai, People's Republic of China*
[9]*Helsinki Institute of Physics, University of Helsinki, 00014 Helsinki, Finland*
[10]*CNR-SPIN c/o Dipartimento di Scienze Fisiche e Chimiche, Università degli Studi dell'Aquila, 67100 L'Aquila, Italy*

(Received 2 August 2023; accepted 11 April 2024; published 5 August 2024)

Sodium iodide (NaI)-based cryogenic scintillating calorimeters using quantum sensors for signal readout have shown promising first results toward a model-independent test of the annually modulating signal detected by the DAMA/LIBRA dark matter experiment. The COSINUS Collaboration has previously reported on the first above-ground measurements using a dual-channel readout of phonons and light based on transition edge sensors (TESs) that allows for particle discrimination on an event-by-event basis. In this article, we outline the first underground measurement of a NaI cryogenic calorimeter readout via the novel remoTES scheme. A 3.67 g NaI absorber with an improved silicon light detector design was operated at the Laboratori Nazionali del Gran Sasso, Italy. A significant improvement in the discrimination power of e^-/γ events to nuclear recoils was observed with a fivefold improvement in the nuclear recoil baseline resolution, achieving $\sigma = 441$ eV. Furthermore, we present a limit on the spin-independent dark matter nucleon elastic scattering cross section, achieving a sensitivity of $\mathcal{O}(\mathrm{pb})$ with an exposure of only 11.6 g d.

DOI: 10.1103/PhysRevD.110.043010

I. INTRODUCTION

Dark matter (DM) detection remains one of the crucial experimental challenges of present-day particle physics and cosmology. Direct DM searches aim to detect potential DM particle candidates via interactions in Earth-bound detectors, but most direct detection efforts have returned null results thus far. In contrast, the DAMA/LIBRA experiment observes an annual modulation of the interaction rate in sodium iodide (NaI) crystals with a statistical significance of 13.7σ [1], a characteristic signature expected from such DM candidates. Yet, the DAMA signal could so far neither be confirmed by any other experiment nor be explained by a non-DM origin.

With the advent of new detection techniques, the direct detection community has made significant progress in pushing the sensitivity for DM-nucleus interactions. Today, cryogenic detectors (CRESST-III [2], EDELWEISS [3], and SuperCDMS [4]) compete for the lowest thresholds, while highest exposures are reached using liquid noble gas detectors (LZ [5], Panda-X [6], and XENONnT [7]). Despite numerous experiments covering

*Corresponding author: mukund@mpp.mpg.de
†Corresponding author: leonie.einfalt@oeaw.ac.at
‡Corresponding author: moritz.kellermann@mpp.mpg.de

the parameter space compatible with the DAMA/LIBRA signal under standard assumptions [8], the origin of the modulated signal remains to be conclusively proven. To reduce the systematic uncertainties of comparing different materials, multiple experiments using the same target material as DAMA/LIBRA are under construction (PICO-LON [9] and SABRE [10]) or already taking data (ANAIS [11], COSINE-100 [12], and DM-Ice [13]).

The COSINUS (cryogenic observatory for signatures seen in next-generation underground searches) experiment utilizes NaI-based scintillating calorimeters operated at cryogenic temperatures and readout using transition edge sensors (TESs). By measuring the scintillation light as well as the phonon signal of atomic recoils, the COSINUS experiment is the only NaI-based experiment able to discriminate the interaction type on an event-by-event basis. Furthermore, it is possible to perform *in situ* measurements of the quenching factor, setting the signal region for recoils off Na and I.

With one year of data taking, first results on a possible nuclear recoil origin of the DAMA/LIBRA signal are anticipated, while 1000 kg d will provide a complete model-independent cross-check [14,15].

In 2021, COSINUS developed the remoTES detector design to build low-threshold detectors for materials so far not operable as cryogenic detectors in a reliable and reproducible way for future mass production [16]. A follow-up study devoted to the application of this design to NaI, a highly challenging absorber crystal for cryogenic searches, was successfully carried out, observing particle discrimination on an event-by-event basis in a NaI experiment for the first time [17]. The study reported here describes an improved detector design operated in an underground cryostat at the Laboratori Nazionali del Gran Sasso (LNGS), yielding the best energy resolution achieved by a NaI-based detector for nuclear recoils. Section II describes the detector module design, which includes a NaI phonon channel with remoTES readout and a silicon (Si) light channel with TES readout. Section III details the experimental setup and Data Acquisition System (DAQ) used for data taking, and Sec. IV describes a simulation done with Geant4 to estimate the expected neutron rate during calibration periods. In Secs. V and VI, the collected data are analyzed, and the resulting DM-nucleon scattering cross-section limit for this measurement is presented.

II. DETECTOR MODULE

The detector module consists of two independent channels: a NaI absorber operated as a cryogenic calorimeter (phonon channel) and a light absorber to detect the corresponding scintillation photons generated by a particle interaction in NaI (light channel). A schematic breakdown of the module is depicted in Figs. 1 and 2.

The phonon channel consists of a 3.67 g NaI crystal mounted in a holder fabricated from electrolytic tough pitch

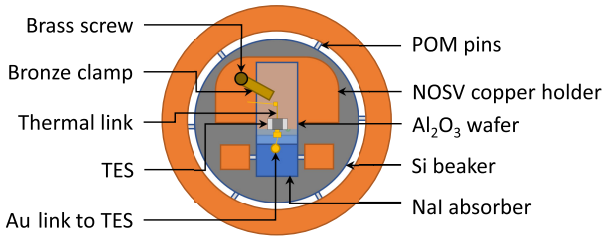

FIG. 1. Top view of the detector module.

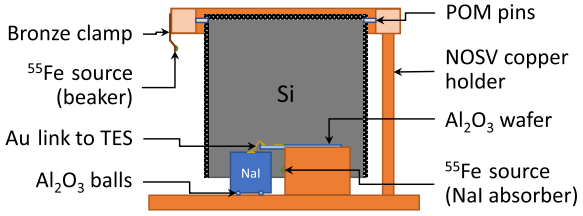

FIG. 2. Cross-sectional view of the detector module.

(NOSV) copper (Cu) [18]. The NaI crystal was produced by Shanghai Institute for Ceramics, China (SICCAS) with a modified Bridgman technique as described in [19] using "Astro-Grade" powder procured from Merck group [20]. Inductively coupled plasma mass spectrometry measurements performed at LNGS [21] revealed an internal contamination at a level of 6–22 ppb for ^{40}K and < 1 ppb for ^{208}Th and ^{238}U. The crystal used for this particular measurement had a thallium (Tl)-dopant level of 730 ± 73 ppm.

The crystal rests on a trio of Al_2O_3 balls to thermally insulate it from the Cu holder. Two additional support tips made out of polyoxymethylene (POM) fix the crystal's position. An ^{55}Fe x-ray source with an activity of 0.11 Bq is taped onto the Cu holder such that it irradiated one of the faces of the crystal. The resultant K_α and K_β lines are

TABLE I. Properties of the phonon channel.

Component	Properties
NaI absorber	Volume: $(10 \times 10 \times 10)$ mm^3
Au link	Au pad on NaI
	Area: 1.77 mm^2
	Thickness: 1 μm
	Glue: EPO-TEK 301-2 [23]
	Au wire
	Length: ∼10 mm
	Diameter: 17 μm
Al_2O_3 wafer	Volume: $(10 \times 20 \times 1)$ mm^3
W-TES on wafer	Area: (100×400) μm^2
	Thickness: 156 nm
	T_C: 28 mK
Heater on wafer	Area: (200×150) μm^2
	Thickness: 100 nm gold

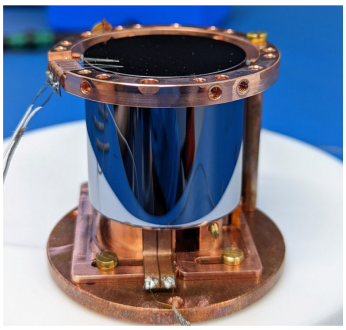

FIG. 3. Photograph of the assembled detector module, consisting of the phonon and light channels.

used to calibrate the detector response in the offline analysis. The remoTES scheme, outlined in [22] and implemented in [16], utilizes a gold (Au) link for signal readout via the TES from particle interactions within the absorber. For the present study, this link consists of an Au pad adhered to NaI, with a thin Au wire connecting the pad to the TES. All components of the phonon channel and their properties are shown in Table I. The TES consists of a tungsten-based superconducting thin film evaporated onto an Al_2O_3 wafer using infrastructure and technology of the CRESST group at the Max-Planck Institute for Physics (MPP) in Munich, Germany. A gold stripe (thermal link) connecting the TES to the thermal bath is used for weak thermal coupling (65 Ω at room temperature) to slowly dissipate heat. An Ohmic heater film was deposited onto the wafer to adjust the TES temperature to the optimal operation point. Externally injected "test pulses" at regular intervals via the heater serve to precisely measure the detector response over its entire dynamic range and to monitor potential changes with time.

Assembly of the module took place in a moisture-regulated nitrogen glovebox (<50 ppm) to avoid degradation of the NaI(Tl) crystal.

With the help of a Cu pillar, the Si beaker is positioned to enclose the NaI crystal as depicted in Fig. 2. A photograph of the complete, dual-channel system is shown in Fig. 3.

TABLE II. Properties of the light channel.

Component	Properties
Si absorber	Hollow cylinder Height: 40 mm Outer diameter: 40 mm Thickness: 1 mm
W-TES on Si	Area: (100 × 400) μm^2 Thickness: 80 nm T_C: 28 mK
Heater on Si	Area: (200 × 150) μm^2 Thickness: 100 nm gold

To collect the scintillation light, a beaker-shaped Si crystal with a mass of 15.38 g was used. It was mounted on a separate Cu frame with the help of six POM tips (applying even pressure from all sides). An ^{55}Fe x-ray source with an activity of 3.3 mBq was taped onto the Cu holder to irradiate the beaker. A tungsten TES was deposited directly on the Si beaker. To efficiently collect athermal phonons and deliver their energy, it is flanked by two superconducting aluminum phonon collectors [24]. A thermal link (15.8 Ω at room temperature) and a separate heater were also deposited on the Si beaker, similar to the scheme described for the phonon channel TES. All components of the light channel and their features are shown in Table II.

III. MEASUREMENT SETUP AND DAQ

The measurement was carried out at LNGS in a $^3He/^4He$ dilution refrigerator of type MINIKELVIN 400-TOF from Leiden Cryogenics B.V. [25] provided by the CRESST group of the Max-Planck Institute for Physics. It is located underground in a side tunnel between hall A and hall B at LNGS with an overburden of 3600 m w.e. [26]. Two superconducting quantum interference devices manufactured by Applied Physics Systems [27] are used for signal amplification [28].

The refrigerator is equipped with an external Pb shield with a thickness of 100 mm. A cylindrical internal radiation shield made from low-background lead (Pb) with a diameter of 90 mm and a thickness of 100 mm is mounted above the detector module. To decouple the sensors from vibrations, the detector module was appended on a bronze (CuSn6) spring with a resonance frequency of a few hertz. The thermalization of all parts was ensured by screwed Cu-wire connections to the mixing chamber. A photograph of the mounting scheme is shown in Fig. 4.

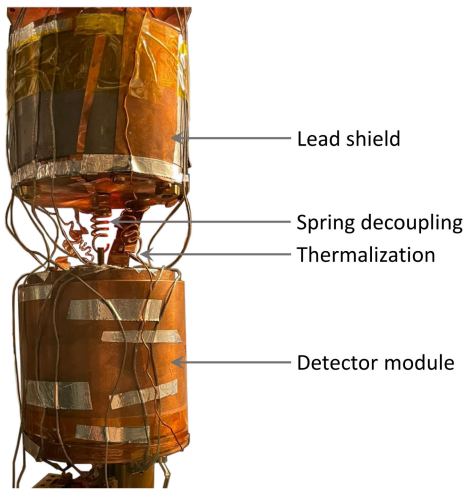

FIG. 4. Photograph of the detector module mounted onto the mixing chamber of the dilution refrigerator.

The detector signals were read out in parallel with two separate systems at a sampling rate of 50 kS/s, a commercial, hardware-triggered DAQ, and a custom-made continuous DAQ. To set up and stabilize the detectors, the hardware-triggered DAQ was used. In total, about ten days of stream data were taken over the first two weeks of June, 2022. Sixteen hours were measured with an external ^{57}Co γ source (122 keV) with an activity of 430 Bq located inside the external lead shield. About 26 hours were measured with an AmBe neutron source with an activity of 2000 Bq located outside the external lead shield. With a background data-taking period lasting for 76 h, an overall exposure of 11.6 g d was collected.

IV. SIMULATION STUDY

To estimate the expected neutron interaction rate in the phonon channel for the measurement with the AmBe source, a Geant4 (v11.0)-based simulation [29–31] of the setup was carried out. The simulated geometry includes the detector module, the vacuum chambers and helium bath of the refrigerator, and the external lead shield. A top view of the setup as implemented in the software is shown in Fig. 5.

In the simulation, an isotropically emitting, pointlike neutron source with an activity of 2000 neutrons/s was placed outside the external lead shielding, including an additional 1 cm of polyethylene between the external Pb shield and the source. The height of the source was varied in 5 cm increments to the detector plane, as the source's precise position with respect to the detector module could not be determined during the run. For each position of the neutron source, five simulations with different seeds were computed. The expected position-dependent neutron rate above a given threshold can then be calculated from mean and standard deviation of these five simulations. To validate the data analysis, the simulated neutron rate can be compared to the measured rate in an energy range which is clearly above threshold (8 keV). The measured neutron rate is calculated by subtracting the rate in the background files, after analysis cuts (described in the next section), from the rate of the neutron calibration data after analysis cuts.

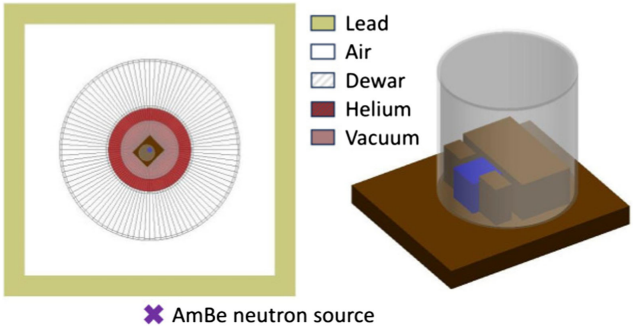

FIG. 5. Geometry as simulated in Geant4. On the left: top view on the refrigerator. On the right: 3D view of the simulated detector module.

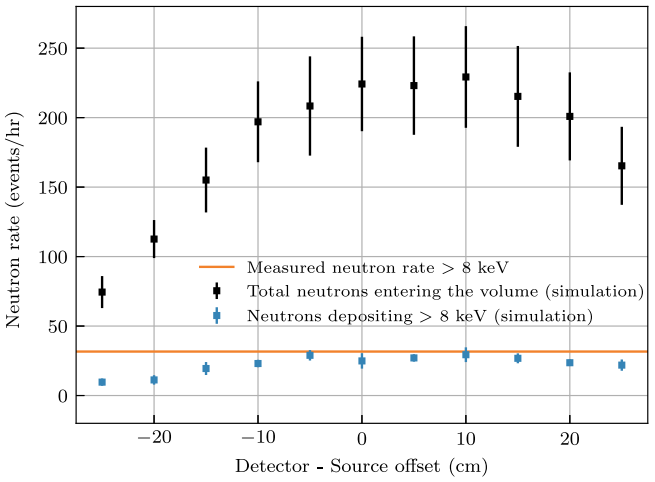

FIG. 6. Simulated and measured neutron rates in the phonon channel.

The rates from simulation and measurement agree and are displayed in Fig. 6.

V. DATA ANALYSIS

A. Raw data analysis

The data used in the subsequent analysis was acquired with the continuous DAQ system, using offline triggering with an optimum filter (OF) trigger on the continuous stream [32]. Two components are needed to calculate the OF for each channel: a representative noise power spectrum (NPS) of the detector and the pulse shape of the events of interest in the respective channel. For the detector NPS, several hundred empty and cleaned noise traces were collected from the hardware-triggered (HWT) background data, and their respective NPS were averaged. From the same HWT background data, a common set of pulses for both channels is selected from a narrow energy region, summed up, and rescaled to get a first estimate of the so-called standard event (SE). The SEs are then fitted with the pulse model described in [33] to eliminate any remaining noise. In a remoTES detector, we expect different pulse shapes attributed to different detector parts [16]. As we are interested in recoil events taking place in the NaI crystal, we use only *absorber events* for generating the SEs and in the subsequent analysis steps. The trigger threshold was determined employing the method described in [34], using empty and cleaned noise traces from the HWT data. With the criterion of one noise trigger per kg d exposure, we fix the trigger threshold at 2 mV in the phonon and 6 mV in the light channel.

A set of quality cuts was applied, aiming to discard pulse shapes different from the SE, artifacts caused by interference, as well as noise triggers. The majority of these cuts affect only the phonon channel. The OF amplitude is used to reconstruct the amplitude of the pulses. Moreover, the

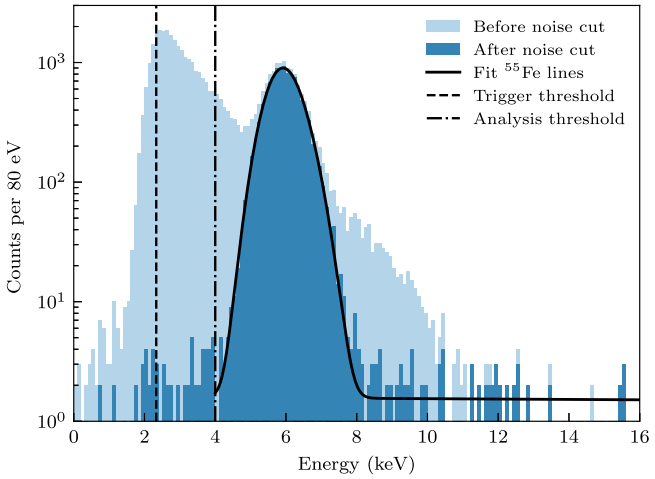

FIG. 7. The energy spectrum of the background dataset below 16 keV before (light blue) and after the noise-leakage removal cut (blue). The black dashed line marks the threshold used for the optimum filter trigger, and the black dash-dotted line the threshold that was used in the subsequent analysis steps. A fit to the ^{55}Mn K_α (5.89 keV) and K_β (6.49 keV) lines gives the solid black line, yielding a resolution of the detector at these energies of 0.450 ± 0.007 keV.

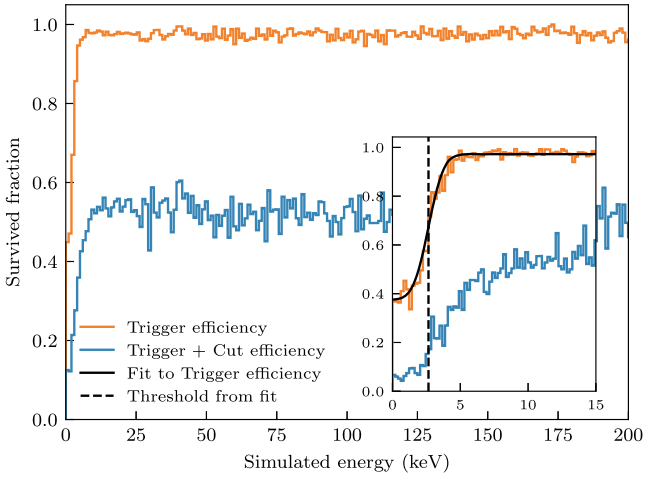

FIG. 8. The orange line shows the trigger efficiency, and the blue line the trigger and cut efficiency as determined from simulated pulses. In the inset, we show an enlargement to lower energies, showing also an error function fit to the trigger efficiency (solid black line), which can be used to estimate the detector threshold to 2.656 ± 0.041 keV (dashed black line).

amplitudes are corrected for small drifts in the detector response over time using the test pulses.

We want to describe one cut performed on the phonon channel in more detail. Although the software trigger thresholds determined above should ensure only minimal leakage of noise events over the threshold, there is a significant accumulation of events visible in the phonon channel close to the triggering threshold, shown in Fig. 7. Because of the non-Gaussian shape of this noise distribution, we assume that the method in [34] is not entirely applicable to our prototype measurement, and the point of one noise trigger per kg d would be at a higher voltage. At low energies, one expects that the reconstruction of a true particle pulse amplitude with an optimum filter should yield the same result as fitting a SE to the pulse. To remove the noise leakage and maintain a low analysis threshold, we compare these two amplitudes for the pulses in the phonon channel and disregard any events where the values differ more than 20%. As can be seen in Fig. 7, this cut removes the majority of noise events, while leaving events from the iron line untouched.

The energy calibration in both channels is performed by fitting a double Gaussian peak to the ^{55}Mn K_α (5.9 keV) and K_β (6.5 keV) lines of the built-in ^{55}Fe x-ray sources (see also Fig. 7). As the iron lines are close to threshold in both light and phonon channels, an additional calibration was performed with a ^{57}Co γ source (122 keV). A slight nonlinearity between the two points of calibration was observed, which can be attributed to a nonlinear detector response at high deposited energies. For energy depositions above a certain magnitude, the connected TES can be heated up close to its normal conducting phase. Since the transition curve of the TES flattens at this point, the resulting pulse shape is distorted, and amplitude reconstruction with the optimum filter becomes infeasible. In order to avoid energies outside the linear range of the detector, we limit the region of interest (ROI) to a maximum energy of 200 keV in both channels.

The cuts described aim at eliminating only artifacts, noise, and pulses of shape different from the events of interest. However, there is still an energy-dependent probability of whether a valid event passes the triggering procedure and the subsequent analysis steps. We evaluate the trigger and cut survival probabilities by applying the whole analysis chain to $\mathcal{O}(10000)$ artificial events. In Fig. 8, we illustrate the results of this procedure. We show the binned fraction of triggered artificial events in the phonon channel, after removing artificial pileups, in black, and the fraction of events additionally surviving the subsequent analysis chain in blue. An extended error function is fitted to the trigger efficiency (orange line):

$$\mathrm{eff}_{\mathrm{trigger}}(E) = c\left((1-\epsilon) \times 0.5\mathrm{erf}\left(\frac{(E-t_p)}{\sqrt{2}\sigma}\right) + \epsilon\right), \quad (1)$$

where c, ϵ, σ, and t_p are free parameters. The fit resulted in a detector threshold of $t_p = 2.656 \pm 0.041$ keV.

To determine the baseline resolution, we superimpose the SE particle template upon cleaned, empty noise traces picked at random times from the full stream. Fitting a Gaussian to the distribution of the filtered amplitudes of these simulated events estimates the resolution as $\sigma_p = 0.3779 \pm 0.0086$ mV/0.441 ± 0.011 keV in the phonon and $\sigma_l = 0.930 \pm 0.021$ mV/0.988 ± 0.052 keV electron

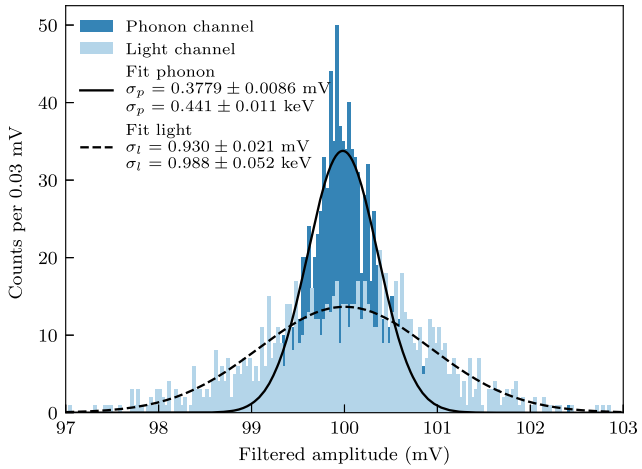

FIG. 9. Histogram of the filtered amplitudes of simulated pulses in both phonon (blue) and light channels (light blue), used to determine the detector baseline resolutions. The solid (dashed) line is a fit of a Gaussian to the phonon (light) channel data, the width of which gives a measure of the baseline resolution.

equivalent ($\mathrm{keV_{ee}}$) in the light channel [34], as shown in Fig. 9. At approximately 5 times the baseline resolution, the above estimate of the threshold agrees well. For practical purposes of this prototype measurement, in all the following steps, we set the analysis threshold to $E_{\mathrm{thr}} = 4$ keV, a value at which the cut efficiency has reached about 50% of its plateauing value.

B. High-level analysis

For an event with light yield $LY = E_l/E_p \neq 1$, the energy in the phonon channel E_p is not a direct measure of the total energy deposited in the target crystal, as a fraction of the energy is dissipated into scintillation light E_l. As both phonon and light energy are measured, we calculate the total deposited energy as $E = \eta E_l + (1-\eta)E_p$ [35]. The correct value of η is determined by gradually increasing η, applying the shift to the data, and fitting a double peak function to the iron lines in Fig. 7. The correct value for η is then the one for which the fitted resolution of the iron lines is minimal. Minimizing the width of the calibration peaks is equivalent to correcting the tilt in the energy-light yield plane described in [35]. With this method, we estimate a scintillation efficiency η of 9.1% and a resolution of the detector at the position of the iron lines of 0.450 ± 0.007 keV, which agrees with the baseline resolution. Following the results of the low-level analysis, the region of interest ROI is set to [4, 200] keV in total deposited energy E. Moreover, we restrict the light yield LY to $[-10, 10]$.

The novel feature of COSINUS, compared to other DM searches with NaI target materials, is the combination of phonon and light signals which is used to discriminate between e^-/γ and nuclear recoil events via their different light yield. Figure 10 displays the light yield vs energy scatter plot for both background and neutron calibration data. The quenched nuclear recoil events in the neutron calibration are clearly separable from the bulk of the e^- and γ recoil events. In Fig. 11, this separation is illustrated down to low energies. Under the assumption that DM particles will mainly recoil off nuclei, the acceptance region for the DM analysis (employing Yellin's optimum interval method [36,37]) is dependent on the position of the nuclear recoil bands in Fig. 10. The positions of the e^-, γ, and nuclear recoil bands are determined by an unbinned likelihood fit to the whole dataset (background and neutron calibration), in both phonon and light energy simultaneously. The parametrization of the energy spectra and quenching factors is based on [38]. The minimization of the total likelihood function was performed using iminuit [39], the PYTHON

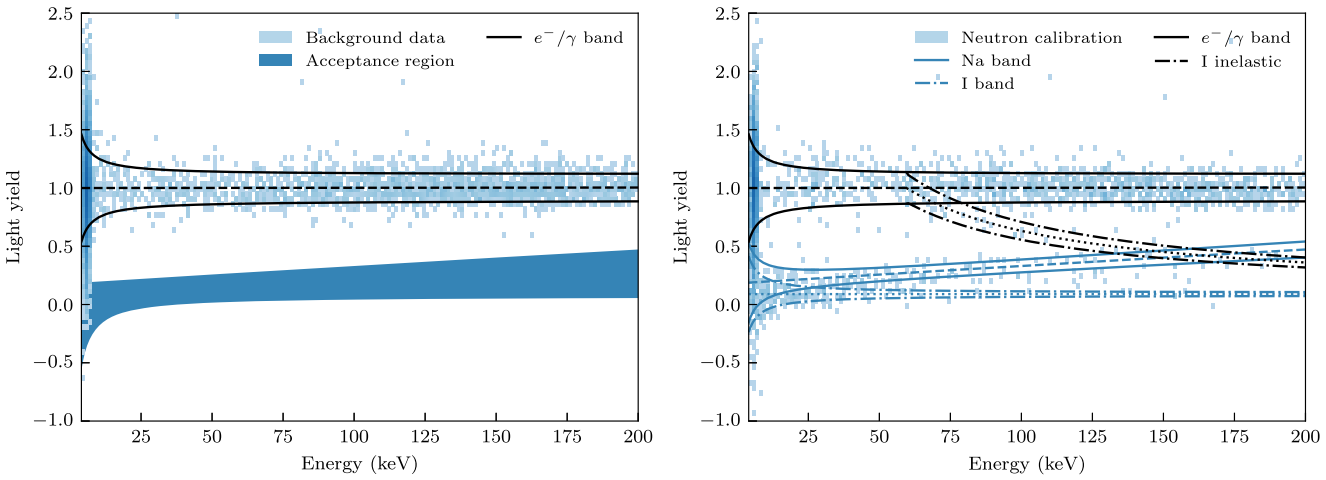

FIG. 10. A 2D histogram of light yield vs the total deposited energy for both background (left) and neutron calibration data (right). Both figures show the fit to the e^-/γ band (black) as found by the combined likelihood fit. Together with the neutron calibration data, we also show the fit results for the nuclear and inelastic recoil bands. The blue shaded region in the left panel marks the acceptance region for DM inference with the Yellin method.

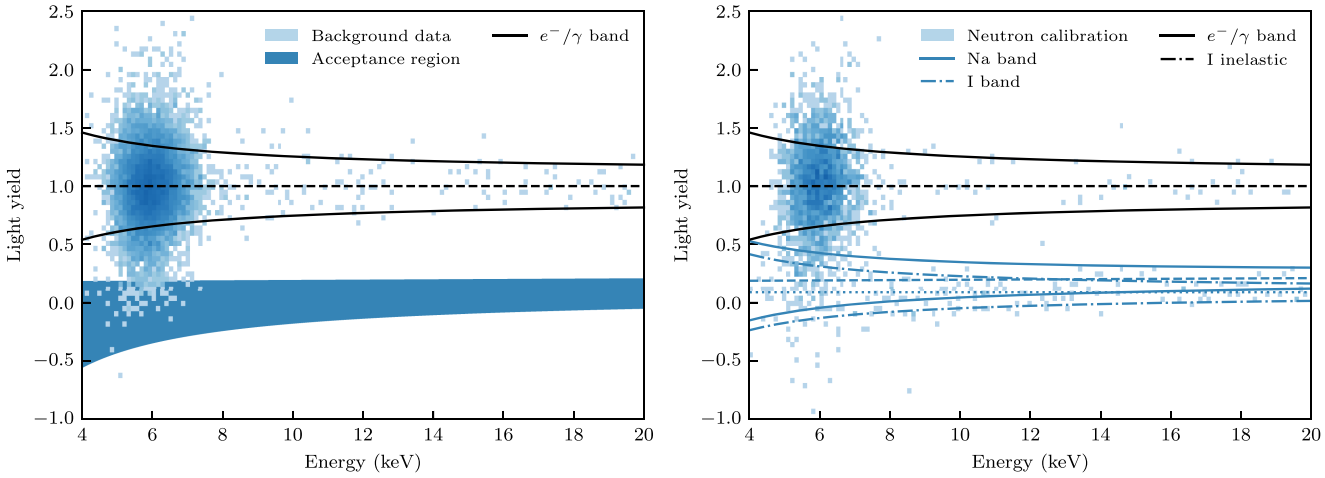

FIG. 11. Enlargement to low energies of Fig. 10.

implementation of the Minuit framework [40]. In addition to the light yield vs energy plot in Fig. 10, Fig. 12 illustrates the performance of the fit in the context of the energy spectra. The selected background model consists of a decreasing flat background, the ^{55}Fe calibration lines (at 5.89 keV and 6.49 keV), and elastic and inelastic nuclear scattering events, as well as a bumplike description of events caused by δ electrons created by charged high-energy particles interacting with the surrounding of the detector (labeled "Compton" in Fig. 12). The model provides a reasonably good representation of the measured data. We want to note that a full model necessitates further studies and simulations to better understand the possible backgrounds associated with the detector.

For the nuclear band n, we describe the quenching factor as $QF_n(E) = E_{l,n}(E)/E_{l,e^-}(E)$, where $E_{l,n}(E)$ is the energy-dependent mean light of the nuclear recoil band and $E_{l,e^-}(E)$ the mean light for electron recoils. Per definition, the mean light yield of the electron band is one at the calibration energy, and we introduce a linear, energy-dependent description to account for detector effects. We note here that we did not observe any nonproportionality in the scintillation light output. We define the fit functions for the light output as follows:

$$E_{l,e^-}(E) = l_0 E + l_1 E^2, \tag{2}$$

$$E_{l,n}(E) = (l_0 E + l_1 E^2) \times k_{QF,n}(1 - a_n e^{-E/d_n}). \tag{3}$$

The variables l_0, l_1, $k_{QF,n}$, a_n, and d_n are free parameters determined from the fit. Using Eqs. (2) and (3), we can directly extract the energy-dependent quenching factors from the result of the likelihood fit. We determined the quenching factors at 10 keV nuclear recoil energy as $QF_{\mathrm{Na}}(10\ \mathrm{keV}) = 0.197 \pm 0.019$ and $QF_{\mathrm{I}}(10\ \mathrm{keV}) = 0.0892 \pm 0.0037$. We want to highlight that the quenching

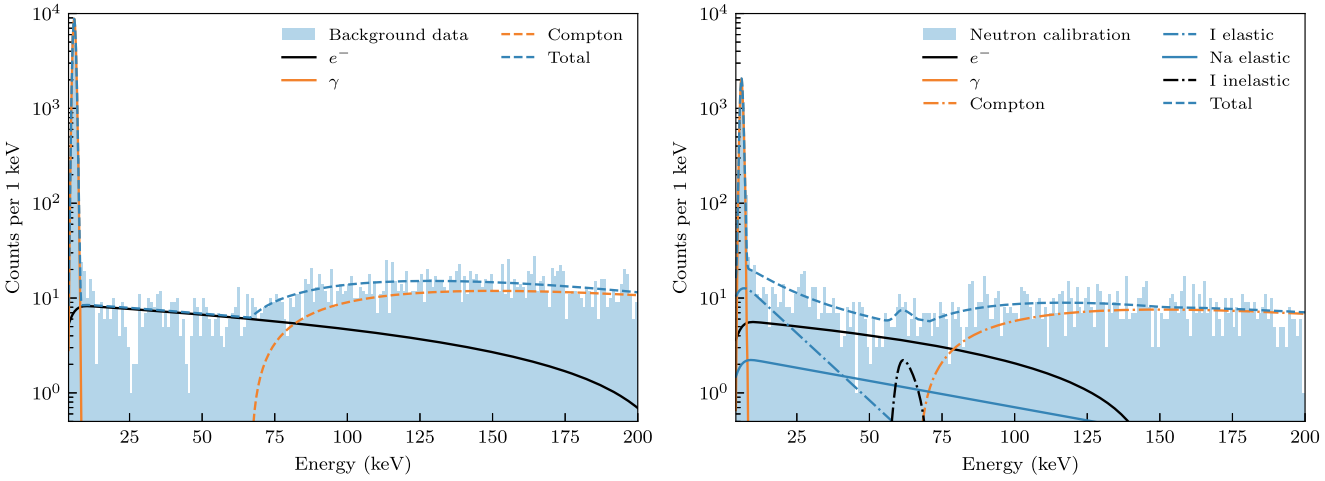

FIG. 12. Energy spectra (total energy, shift corrected) of the ROI for both background (left) and neutron calibration data (right). The plots also show the parametric descriptions of the energy spectra as yielded by the combined likelihood fit.

TABLE III. Fit values of the parameters necessary to describe the energy-dependent light quenching of the nuclear recoil bands in Eq. (2) as acquired by the maximum likelihood fit. The last two rows state the values of the quenching factors for sodium and iodine at 10 keV total deposited energy.

Parameter	Fit value
l_0	0.8131 ± 0.0026
l_1	$8.98 \times 10^{-4} \pm 0.28 \times 10^{-5}$ keV^{-1}
$k_{QF,\mathrm{Na}}$	2.864 ± 0.079
a_{Na}	0.9197 ± 0.0032
d_{Na}	$1.91 \times 10^3 \pm 0.12 \times 10^3$ keV
$k_{QF,\mathrm{I}}$	0.1005 ± 0.0041
a_{I}	680 ± 450
d_{I}	0.071 ± 0.031 keV
$QF_{\mathrm{Na}}(10\ \mathrm{keV})$	0.197 ± 0.019
$QF_{\mathrm{I}}(10\ \mathrm{keV})$	0.0892 ± 0.0037

factors are measured intrinsically and specifically for this crystal, such that uncertainties stem purely from the fit. One interesting observation we made in the analysis of this measurement is that the light yield of the nuclear recoil events increases toward higher deposited energies. This behavior is contrary to observations made in other materials, such as $CaWO_4$ [41]. Together with the quenching factors at 10 keV, other results from the fit are noted in Table III.

Using the results from the fit, we then define the acceptance region as the area in the energy-light yield plane between the mean of the sodium and the 99.5% lower limit of the iodine band. The acceptance region is marked in blue in Fig. 10. From the likelihood fit, we estimate the leakage from the e^-/γ band into the acceptance region to $0.48 \pm 0.11\%$ between 4 and 6 keV and $(6.7 \pm 2.3) \times 10^{-4}\%$ between 6 and 200 keV. Considering the background level in the described dataset, this corresponds to a leakage of 1 count/(keV g d) and 1.5×10^{-5} counts/(keV g d), respectively. We note here that the exponential description of the energy-dependent light yield for the nuclear recoil band is purely phenomenological. To ensure that the parametrization of the nuclear recoil bands does not affect the DM analysis, we performed the whole high-level analysis chain with various descriptions of the energy-dependent light quenching, all leading to comparable limits.

VI. DARK MATTER RESULT

To give a comparable measure of the detector performance and the impact of the event-by-event discrimination on a DM analysis, we use the background dataset to obtain limits on the nucleon-DM spin-independent elastic scattering cross section. The expected DM interaction rate $\frac{dR_{\mathrm{det}}}{dE}$ as observed by the detector is characterized by the standard spin-independent scattering model. It includes detector-specific quantities such as the threshold E_{thr}, the trigger,

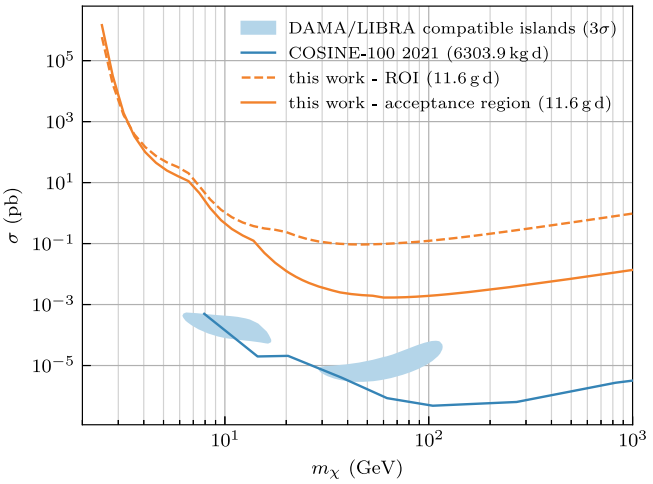

FIG. 13. 90% confidence level upper limit on the spin-independent, elastic nucleon-DM scattering cross section in the standard scenario, σ(pb) as a function of the DM mass, m_χ. The orange lines show the results of this work from a background dataset with 11.6 g d of exposure. The dashed line is the limit achieved considering all events in the ROI; for the solid line, only the events in the acceptance region were considered. As a comparison, we show contours compatible with the DAMA/LIBRA result [46] and the COSINE-100 result from 6303.9 kg d exposure [47], a factor $\sim 10^5$ higher than the current study.

and cut efficiency $\varepsilon(E)$, as well as the probability $p_{\mathrm{ACR}}(E)$ that a DM recoil event lies within the acceptance region. The resolution of the phonon channel is dominated by the Gaussian baseline noise and, therefore, taken into account by convolution with a Gaussian Ga of width σ_p:

$$\frac{dR_{\mathrm{det}}}{dE}(E) = \theta(E - E_{\mathrm{thr}})\varepsilon(E)p_{\mathrm{ACR}}(E) \times \int_0^\infty \frac{dR_{\mathrm{theo}}}{dE'}(E')Ga(E - E', \sigma_p^2)dE'. \quad (4)$$

The theoretical model $\frac{dR_{\mathrm{theo}}}{dE'}$ is based on the standard assumptions for an isothermal DM halo [8]. Effects of the nuclear shape for the sodium and iodine nuclei are modeled by the Helm (extended by Lewin and Smith) form factor [42,43], while the low contribution of Tl is conservatively considered negligible in the calculation.

Using Yellin's optimum interval method [36,37], we obtain the 90% confidence level upper limits displayed in Fig. 13. Besides the limit calculated from the acceptance region (solid line), we also show the limits calculated from all data points in the ROI (dashed line). A comparison of the two lines shows that COSINUS' unique event-by-event discrimination enables to set an up to 2 orders stricter limit in the standard scenario. We emphasize that the limits from the acceptance region with 11.6 g d of exposure are only 3 orders of magnitude less strict than the limits from COSINE-100 with 6303.9 kg d exposure (blue line) shown for comparison. In addition, we note that the sensitivity of the prototype was limited due to leakage from the e^-/γ band

to the nuclear recoil bands. The majority of these leakage events stem from the ^{55}Fe calibration source (compare with Fig. 11), as well as the overall e^-/γ background present in the dilution refrigerator. We count 11111 events in the energy interval [4, 8] keV, and the likelihood fit assigns 11070 ± 140 events to the iron lines in this energy range. We will have a significant improvement for such measurements in the final low-background facility of COSINUS [44]. This is also directly related to the convergence of the limits from the acceptance region (solid orange line) and the ROI (dashed orange line) at lower DM masses, which correspond to lower energies where the discrimination power is reduced. Thus, we expect a profile-likelihood ratio approach for the DM analysis, instead of the Yellin method, to further improve the sensitivity [45].

VII. CONCLUSION

In this work, we present the results of the first underground operation of a NaI-based cryogenic scintillating calorimeter. A baseline resolution of 0.441 keV for nuclear recoils was achieved for the phonon channel. Together with the Si-based light channel, the dual-channel readout was operated successfully, enabling particle discrimination between e^-/γ and nuclear recoils on an event-by-event basis. Based on these results, we determine the energy-dependent quenching factors for sodium and iodine as observed in the operated crystal to $QF_{\mathrm{Na}}(10\ \mathrm{keV}) = 0.197 \pm 0.019$ and $QF_{\mathrm{I}}(10\ \mathrm{keV}) = 0.0892 \pm 0.0037$, respectively. Furthermore, we give limits on the standard spin-independent, elastic scattering cross section, based on 11.6 g d exposure of this R&D run's background dataset, demonstrating how our unique background discrimination increases the sensitivity of a COSINUS detector with respect to NaI experiments with single-channel readout.

Future R&D campaigns will focus on upscaling the detector design to house undoped NaI crystals of the order of $\mathcal{O}(10g)$, as planned for the final experimental setup of COSINUS, while further lowering the threshold for nuclear recoils.

ACKNOWLEDGMENTS

We thank the CRESST group at the Max Planck Institute for Physics, Munich for allowing us to use their cryogenic test facility at LNGS and detector production infrastructure in Munich, as well as for sharing their cryogenic expertise with us. We are also grateful to LNGS for their generous support and technical assistance in ensuring a smooth run underground. The offline data analysis was mainly carried out with collaboration-internal software tools CAT and limitless and cross-checks partially with the open source PYTHON package CAIT [48]. Additionally, we thank the MPP and HEPHY mechanical workshop teams for their timely assistance in detector holder fabrication. This work has been supported by the Austrian Science Fund FWF, stand-alone project AnaCONDa [Grant DOI:10.55776/P33026-N] and by the Austrian Research Promotion Agency (FFG), project ML4CPD. This project was supported by Research Council of Finland (Grant No. 342777) and Väisälä foundation.

[1] R. Bernabei, P. Belli, A. Bussolotti, V. Caracciolo, R. Cerulli, N. Ferrari *et al.*, Recent results from DAMA/LIBRA and comparisons, Moscow Univ. Phys. Bull. **77**, 291 (2022).
[2] A. H. Abdelhameed *et al.* (CRESST Collaboration), First results from the CRESST-III low-mass dark matter program, Phys. Rev. D **100**, 102002 (2019).
[3] E. Armengaud *et al.* (EDELWEISS Collaboration), Searching for low-mass dark matter particles with a massive Ge bolometer operated above ground, Phys. Rev. D **99**, 082003 (2019).
[4] R. Agnese *et al.* (SuperCDMS Collaboration), Results from the super cryogenic dark matter search experiment at Soudan, Phys. Rev. Lett. **120**, 061802 (2018).
[5] D. S. Akerib *et al.* (LUX-ZEPLIN Collaboration), Projected sensitivity of the LUX-ZEPLIN experiment to the two-neutrino and neutrinoless double β decays of ^{134}Xe, Phys. Rev. C **104**, 065501 (2021).
[6] X. Ning *et al.* (PandaX Collaboration), Limits on the luminance of dark matter from xenon recoil data, Nature (London) **618**, 47 (2023).
[7] E. Aprile *et al.* (XENON Collaboration), Search for inelastic scattering of WIMP dark matter in XENON1T, Phys. Rev. D **103**, 063028 (2021).
[8] D. Baxter *et al.*, Recommended conventions for reporting results from direct dark matter searches, Eur. Phys. J. C **81**, 907 (2021).
[9] K. Fushimi *et al.*, Dark matter search project PICO-LON, J. Phys. Conf. Ser. **718**, 042022 (2016).
[10] M. Antonello *et al.* (SABRE Collaboration), The SABRE project and the SABRE proof-of-principle, Eur. Phys. J. C **79**, 363 (2019).
[11] J. Amaré *et al.* (ANAIS-112 Collaboration), Annual modulation results from three-year exposure of ANAIS-112, Phys. Rev. D **103**, 102005 (2021).
[12] G. Adhikari *et al.* (COSINE-100 Collaboration), Three-year annual modulation search with COSINE-100, Phys. Rev. D **106**, 052005 (2022).
[13] E. Barbosa de Souza *et al.* (DM-Ice Collaboration), First search for a dark matter annual modulation signal with NaI(Tl) in the Southern Hemisphere by DM-Ice17, Phys. Rev. D **95**, 032006 (2017).

[14] G. Angloher *et al.* (COSINUS Collaboration), The COSINUS project: Perspectives of a NaI scintillating calorimeter for dark matter search, Eur. Phys. J. C **76**, 441 (2016).
[15] F. Kahlhoefer, F. Reindl, K. Schäffner, K. Schmidt-Hoberg, and S. Wild, Model-independent comparison of annual modulation and total rate with direct detection experiments, J. Cosmol. Astropart. Phys. 05 (2018) 074.
[16] G. Angloher *et al.* (COSINUS Collaboration), First measurements of remoTES cryogenic calorimeters: Easy-to-fabricate particle detectors for a wide choice of target materials, Nucl. Instrum. Methods Phys. Res., Sect. A **1045**, 167532 (2023).
[17] G. Angloher *et al.* (COSINUS Collaboration), First results on particle discrimination in a NaI crystal using the COSINUS remote TES design, arXiv:2307.11066.
[18] Aurubis, https://www.aurubis.com/ (2024).
[19] Y. Zhu *et al.*, Production of ultra-low radioactivity NaI (Tl) crystals for dark matter detectors, in *Proceedings of the 2018 IEEE Nuclear Science Conference (NSS/MIC)* (IEEE, New York, 2018), pp. 1–3.
[20] Merck Group, https://www.merckgroup.com/ (2023).
[21] S. Nisi, L. Copia, I. Dafinei, and M. L. Di Vacri, ICP-MS measurement of natural radioactivity at LNGS., Int. J. Mod. Phys. A **32**, 1743003 (2017).
[22] M. Pyle, E. Figueroa-Feliciano, and B. Sadoulet, Optimized designs for very low temperature massive calorimeters, arXiv:1503.01200.
[23] Epoxy technology, https://www.epotek.com/ (2024).
[24] G. Angloher *et al.* (CRESST Collaboration), Quasiparticle diffusion in CRESST light detectors., J. Low Temp. Phys. **184**, 323 (2016).
[25] Leiden Cryogenics BV, https://leidencryogenics.nl/ (2024).
[26] M. Ambrosio *et al.*, Vertical muon intensity measured with MACRO at the Gran Sasso laboratory, Phys. Rev. D **52**, 3793 (1995).
[27] Applied Physics Systems, https://appliedphysics.com/ (2024).
[28] K. J. Schäffner, Study of backgrounds in the CRESST dark matter search, Ph.D. thesis, TU Munich, 2013.
[29] S. Agostinelli *et al.*, Geant4—A simulation toolkit, Nucl. Instrum. Methods Phys. Res., Sect. A **506**, 250 (2003).
[30] J. Allison *et al.*, Geant4 developments and applications, IEEE Trans. Nucl. Sci. **53**, 270 (2006).
[31] J. Allison *et al.*, Recent developments in Geant4, Nucl. Instrum. Methods Phys. Res., Sect. A **835**, 186 (2016).
[32] E. Gatti and P. F. Manfredi, Processing the signals from solid state detectors in elementary particle physics, Riv. Nuovo Cimento **9**, 1 (1986).
[33] V. Zema, Unveiling the nature of dark matter with direct detection experiments, Ph.D. thesis, Chalmers U. Tech., 2020.
[34] M. Mancuso, A. Bento, N. F. Iachellini, D. Hauff, F. Petricca, F. Pröbst, J. Rothe, and R. Strauss, A method to define the energy threshold depending on noise level for rare event searches, Nucl. Instrum. Methods Phys. Res., Sect. A **940**, 492 (2019).
[35] G. Angloher *et al.* (CRESST-II Collaboration), Results on low mass WIMPs using an upgraded CRESST-II detector, Eur. Phys. J. C **74**, 3184 (2014).
[36] S. Yellin, Finding an upper limit in the presence of an unknown background, Phys. Rev. D **66**, 032005 (2002).
[37] S. Yellin, Extending the optimum interval method, arXiv:0709.2701.
[38] D. Schmiedmayer, Calculation of dark-matter exclusions-limits using a maximum likelihood approach, 10.34726/hss.2019.63441 (2019).
[39] H. Dembinski *et al.*, scikit-hep/iminuit, https://zenodo.org/records/10638795, 2020.
[40] F. James and M. Roos, Minuit: A system for function minimization and analysis of the parameter errors and correlations, Comput. Phys. Commun. **10**, 343 (1975).
[41] R. Strauss *et al.* (CRESST Collaboration), Energy-dependent light quenching in $CaWO_4$ crystals at mK temperatures, Eur. Phys. J. C **74**, 2957 (2014).
[42] R. H. Helm, Inelastic and elastic scattering of 187-Mev electrons from selected even-even nuclei, Phys. Rev. **104**, 1466 (1956).
[43] J. Lewin and P. Smith, Review of mathematics, numerical factors, and corrections for dark matter experiments based on elastic nuclear recoil, Astropart. Phys. **6**, 87 (1996).
[44] G. Angloher *et al.* (COSINUS Collaboration), Simulation-based design study for the passive shielding of the COSINUS dark matter experiment, Eur. Phys. J. C **82**, 248 (2022).
[45] G. Angloher *et al.*, A likelihood framework for cryogenic scintillating calorimeters used in the CRESST dark matter search, arXiv:2403.03824.
[46] C. Savage, G. Gelmini, P. Gondolo, and K. Freese, Compatibility of DAMA/LIBRA dark matter detection with other searches, J. Cosmol. Astropart. Phys. 04 (2009) 010.
[47] G. Adhikari *et al.*, An experiment to search for dark-matter interactions using sodium iodide detectors, Nature (London) **564**, 83 (2018).
[48] F. Wagner, D. Bartolot, D. Rizvanovic, F. Reindl, J. Schieck, and W. Waltenberger, CAIT—analysis toolkit for cryogenic particle detectors in python, Comput. Software Big Sci. **6**, 19 (2022).